

Decomposing the Drivers of Polar Amplification with a Single-Column Model

MATTHEW HENRY,^a TIMOTHY M. MERLIS,^b NICHOLAS J. LUTSKO,^c AND BRIAN E. J. ROSE^d

^a College of Engineering, Mathematics and Physical Sciences, University of Exeter, Exeter, United Kingdom

^b Department of Atmospheric and Oceanic Sciences, McGill University, Montreal, Quebec, Canada

^c Scripps Institution of Oceanography, University of California at San Diego, La Jolla, California

^d Department of Atmospheric and Environmental Sciences, University at Albany, State University of New York, Albany, New York

(Manuscript received 17 March 2020, in final form 3 December 2020)

ABSTRACT: The precise mechanisms driving Arctic amplification are still under debate. Previous attribution methods compute the vertically uniform temperature change required to balance the top-of-atmosphere energy imbalance caused by each forcing and feedback, with any departures from vertically uniform warming collected into the lapse-rate feedback. We propose an alternative attribution method using a single-column model that accounts for the forcing dependence of high-latitude lapse-rate changes. We examine this method in an idealized general circulation model (GCM), finding that, even though the column-integrated carbon dioxide (CO₂) forcing and water vapor feedback are stronger in the tropics, they contribute to polar-amplified surface warming as they produce bottom-heavy warming in high latitudes. A separation of atmospheric temperature changes into local and remote contributors shows that, in the absence of polar surface forcing (e.g., sea ice retreat), changes in energy transport are primarily responsible for the polar-amplified pattern of warming. The addition of surface forcing substantially increases polar surface warming and reduces the contribution of atmospheric dry static energy transport to the warming. This physically based attribution method can be applied to comprehensive GCMs to provide a clearer view of the mechanisms behind Arctic amplification.

KEYWORDS: Arctic; Climate change; Feedback

1. Introduction

The Arctic amplification of surface temperature change is a robust feature of observations (Stocker et al. 2013) and comprehensive climate model simulations (Pithan and Mauritsen 2014). A number of mechanisms are thought to contribute to Arctic amplification, including the surface albedo feedback, increased atmospheric energy transport convergence (Hwang and Frierson 2010), and temperature feedback (Pithan and Mauritsen 2014); however, the precise contribution of each mechanism is still unclear. Clarifying how these different factors contribute to Arctic amplification is essential for reducing the uncertainty in the rate of Arctic warming through improved process-level understanding.

The tropics differ from the high latitudes in that they are close to radiative–convective equilibrium: heating by convection is balanced by radiative cooling, and the vertical temperature profile is mostly determined by surface temperature and humidity, hence the vertical structure of temperature change in the tropics is largely insensitive to the perturbation type. The high latitudes, on the other hand, are close to radiative–advective equilibrium: warming from horizontal atmospheric heat transport is balanced by cooling from radiation. This means that different forcings and feedbacks induce different lapse-rate responses. For example, an increase in longwave

optical depth leads to bottom-heavy warming (Cronin and Jansen 2016; Henry and Merlis 2020), whereas atmospheric energy transport is thought to primarily affect the midtroposphere at high latitudes (Laliberté and Kushner 2013; Feldl et al. 2017). This implies that the ratio between surface warming and top-of-atmosphere (TOA) net radiation changes at high latitudes is different for each forcing and feedback. Surface temperature change attributions based on TOA budget analyses (Pithan and Mauritsen 2014) compute the vertically uniform temperature change required to balance the top-of-atmosphere energy imbalance caused by each forcing and feedback, with any departures from vertically uniform warming collected into the lapse-rate feedback. In these attributions, the lapse-rate feedback functions as a residual that cannot be clearly ascribed to any particular physical process and can obscure the true drivers of Arctic amplification. Similarly, moist energy balance models (e.g., Roe et al. 2015) assume a linear relationship between changes in surface temperature change and changes in net TOA radiation, and hence do not account for the different vertical structures of the high-latitude temperature responses to CO₂ forcing and to changes in atmospheric energy transport convergence. Feldl et al. (2020) decompose the high-latitude lapse-rate feedback into an upper component driven mainly by poleward atmospheric energy transport and a lower component driven by local sea ice loss. They find an increased contribution to Arctic amplification for the combined albedo and lower lapse-rate feedback, while the combined water vapor and upper lapse-rate feedback contribute equally to tropical and Arctic warming.

The coupled atmosphere surface climate feedback response analysis method (CFRAM) is a vertically resolved version of the previously mentioned TOA energy budget method (Lu and

Supplemental information related to this paper is available at the Journals Online website: <https://doi.org/10.1175/JCLI-D-20-0178.s1>.

Corresponding author: Matthew Henry, m.henry@exeter.ac.uk

Cai 2009). The local radiative response to temperature is linearized to infer the magnitude of the temperature change that balances any energy flux perturbation. Using CFRAM, Taylor et al. (2013) found that an increase in CO₂ and water vapor leads to bottom-heavy warming at high latitudes (their Figs. 2 and 3c) and convection leads to top-heavy warming at low latitudes (their Fig. 8c).

Process-oriented and mechanism-denial experiments are useful tools for studying the mechanisms responsible for Arctic amplification. For example, the analysis from Stuecker et al. (2018) suggests that local forcings and feedbacks dominate the polar-amplified pattern of surface temperature change in a comprehensive GCM in which CO₂ concentrations are increased in restricted latitudinal bands. They find that restricting the CO₂ forcing to high latitudes produces a polar-amplified warming structure, whereas restricting the CO₂ forcing to the tropics or midlatitudes leads to a more latitudinally uniform temperature change. However, this result may be model-dependent: Shaw and Tan (2018) show that restricting the CO₂ forcing to the tropics also leads to a polar-amplified surface temperature change in two different comprehensive climate models with aquaplanet lower boundary conditions. Stuecker et al. (2018) also show that the vertical structure of high-latitude warming depends on where the CO₂ forcing is applied: a midlatitude CO₂ forcing leads to a more vertically uniform warming due to the effect of advection (Laliberté and Kushner 2013), whereas a high-latitude CO₂ forcing leads to a surface-enhanced warming structure. Screen et al. (2012) attribute near-surface warming to local forcings and feedbacks and warming aloft to atmospheric energy transport increases by prescribing local and remote sea surface temperature (SST) and sea ice concentration (SIC) changes in two comprehensive atmospheric GCMs. But, prescribing SST where the model would otherwise warm (or cool) the surface is akin to imposing a surface heat sink (or source), hence the results are not easily interpretable.

While these comprehensive GCM studies provide important insights into the mechanisms of Arctic amplification, a hierarchy of models is required for a complete understanding of the drivers of Arctic amplification in climate models and observations. Previous work using single-column model representations of the high-latitude atmosphere suggested that the high-latitude temperature response is sensitive to the forcing type (Abbot and Tziperman 2008; Payne et al. 2015). Cronin and Jansen (2016) have developed a one-dimensional model of an atmosphere in radiative–advective equilibrium for the high latitudes, which led to the important insight that high-latitude lapse-rate changes are forcing dependent. The present work seeks to bridge the gap between their simple radiative–advective column model and complex climate model simulations in order to advance our understanding of the drivers of Arctic amplification.

Using an idealized moist atmospheric GCM with aquaplanet surface boundary conditions, no clouds, and no sea ice (hence no surface albedo feedback), we qualitatively reproduce the pattern of surface temperature change from comprehensive GCMs in response to quadrupled CO₂. To simulate the effect of melting sea ice, we impose a polar surface heat source, ranging from 0 to 24 W m⁻². Then, we use a single-column model (SCM) to emulate the tropics and high latitudes of the

idealized GCM. This allows us to calculate the response to each individual forcing and feedback and thus decompose the drivers of tropical and polar temperature change. This physically based attribution method does not attribute any warming to the lapse-rate feedback. Instead, each forcing and feedback's surface temperature change attribution already accounts for their impact on the vertical structure of temperature change. The SCM attribution method builds on CFRAM by using a convection scheme, which allows the SCM to be run as an "offline" version of the original GCM, with the exception of horizontal energy transports and changes in heating due to condensation, which still have to be taken from the GCM (or observations). The SCM can then be used to perform feedback-locking experiments, and hence is a valuable tool for untangling the drivers of polar amplification. The idealized GCM acts as a test case for the attribution method, which could potentially be used to untangle the contributions of the various mechanisms of polar amplification in comprehensive models.

2. Idealized atmospheric GCM

We use an idealized moist atmospheric GCM based on the Geophysical Fluid Dynamics Laboratory (GFDL) spectral dynamical core and the comprehensive radiation scheme of the GFDL AM2 GCM, with no sea ice or clouds. This is similar to the setup in Merlis et al. (2013) and to the so-called Model of an Idealized Moist Atmosphere (MiMA; Jucker and Gerber 2017). These GCMs follow the moist idealized GCM described in Frierson et al. (2006), but use comprehensive clear-sky radiation instead of gray radiation. In the MiMA setup, the surface albedo is globally uniform and increased to compensate for the cooling effect of clouds. In Merlis et al. (2013), an idealized cloud distribution is prescribed for the radiative transfer calculation. Here, there are no clouds and we set the surface albedo to a hemispherically symmetric analytic distribution similar to Earth's Northern Hemisphere TOA albedo, as estimated from the Cloud and the Earth's Radiant Energy System (CERES) data (Loeb et al. 2018, see Fig. S1 in the online supplemental material), in order to produce an Earth-like meridional surface temperature gradient. The model uses the comprehensive radiation scheme described in Anderson et al. (2004), with annual-mean solar insolation and a solar constant equal to 1365 W m⁻².

The surface boundary condition is a slab mixed layer ocean aquaplanet with no representation of ocean heat transport and the heat capacity of 1 m of water. We use annual-mean insolation and the small mixed layer depth allows the model to equilibrate quickly without meaningfully affecting the model's climate, as we only consider time-independent boundary conditions and forcing. The GCM was run at T42 spectral truncation, for a nominal horizontal resolution of 2.8° × 2.8°, and with 30 vertical levels. The skin temperature is interactively computed using the surface radiative and turbulent fluxes, which are determined by bulk aerodynamic formulas. A *k*-profile scheme with a dynamically determined boundary layer height is used to parameterize the boundary layer turbulence. The GCM uses a simplified Betts–Miller convection scheme (Frierson 2007), and large-scale condensation is parameterized such that the relative humidity does not exceed 1 and condensed

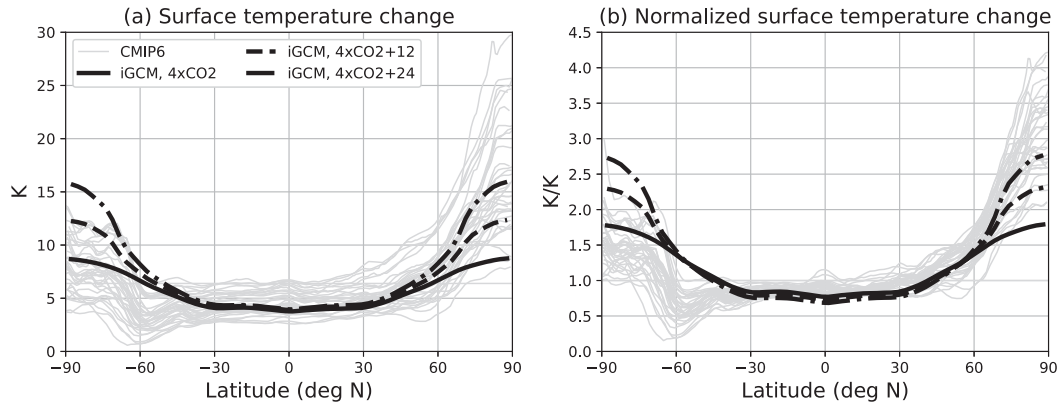


FIG. 1. (a) Surface temperature difference between the control experiment (300 ppm CO_2 concentration) and increased CO_2 experiment (1200 ppm) (black solid) and increased CO_2 experiment (1200 ppm) with a 12 W m^{-2} (black dashed) and 24 W m^{-2} (black dash-dotted) surface heat source poleward of 80° using an idealized moist atmospheric GCM with no clouds or sea ice. These are compared to abrupt $4 \times \text{CO}_2$ surface temperature changes in simulations with the following models from CMIP6: ACCESS-CM2, ACCESS-ESM1-5, AWI-CM1-1-MR, BCC-CSM2-MR, BCC-ESM1, CAMS-CSM1-0, CESM2, CESM2-FV2, CESM2-WACCM, CESM2-WACCM-FV2, CIESM, CMCC-CM2-SR5, CanESM5, EC-Earth3-Veg, FGOALS-f3-L, FGOALS-g3, GFDL-CM4, GFDL-ESM4, GISS-E2-1-G, GISS-E2-1-H, GISS-E2-2-G, INM-CM4-8, INM-CM5-0, IPSL-CM6A-LR, KACE-1-0-G, MCM-UA-1-0, MIROC6, MPI-ESM1-2-HAM, MPI-ESM1-2-HR, MPI-ESM1-2-LR, MRI-ESM2-0, NESM3, NorESM2-LM, NorESM2-MM, SAM0-UNICON, and TaiESM1. (b) As in (a), but the temperature changes are normalized by global-mean surface temperature change.

water is assumed to immediately return to the surface. As there is no representation of sea ice, there is no surface albedo feedback. To mimic the presence of the surface albedo feedback, we run perturbation experiments with an added polar surface heat source. All simulations are run for 20 years with time averages over the last 10 years shown, when all climate states have reached a statistical steady state.

We perform four simulations: a control run in which the atmospheric CO_2 concentration is set to 300 ppm, a run with quadrupled (1200 ppm) CO_2 concentration, and two runs with quadrupled CO_2 concentrations and constant surface heat sources Q_s of 12 and 24 W m^{-2} poleward of 80° in both hemispheres. The heat sources simulate surface heating through the surface albedo feedback or a large increase in oceanic energy transport convergence. Given that the polar surface temperature change under $4 \times \text{CO}_2$ is approximately 8 K, a 12 (24) W m^{-2} surface heat source is equivalent to a 1.5 (3) $\text{W m}^{-2} \text{K}^{-1}$ local feedback. This can be compared to the locally defined surface albedo feedback from the models participating in phase 5 of the Coupled Model Intercomparison Project (CMIP5), which is approximately $1 \text{ W m}^{-2} \text{K}^{-1}$ in the Arctic and $2 \text{ W m}^{-2} \text{K}^{-1}$ in the Southern Ocean (Feldl and Bordoni 2016, their Fig. 1). We note that the polar surface heat source is not comparable to the annual-mean surface heat flux anomaly from comprehensive models, which includes changes in the other terms of the surface energy budget.

Figure 1a shows the zonal-mean surface skin temperature differences between the control and three perturbation simulations, in addition to the zonal-mean surface skin temperature responses of abrupt $4 \times \text{CO}_2$ experiments with models participating in phase 6 of the Coupled Model Intercomparison Project (CMIP6) (Eyring et al. 2016), averaged over 50 years after 100 years of integration. Figure 1b shows the surface

temperature changes normalized by their global mean. The patterns of surface temperature change from the idealized model experiments (black) approximately span the CMIP6 model responses (gray). The amount of Arctic amplification is smaller in the idealized GCM's $4 \times \text{CO}_2$ experiment due to the lack of local positive feedbacks such as sea ice and cloud feedbacks. However, adding a polar surface heat source brings the idealized GCM closer to CMIP6 in the Arctic, which have high latitude warming of 2 to 4 times the global-mean surface temperature change. Note that the CMIP6 temperature changes are not fully equilibrated, and, at equilibrium, the Antarctic is also expected to have amplified warming, but this warming is transiently delayed by upwelling in the Southern Ocean (Manabe et al. 1991; Rugenstein et al. 2019).

3. Single-column model

To emulate the tropical and high-latitude atmosphere of the idealized GCM, we use the single-column model (SCM) from the ClimLab Python package for process-oriented climate modeling (Rose 2018). The atmospheric and surface temperature tendency budgets are given by

$$\frac{\partial T_{\text{atm}}(p)}{\partial t} = \frac{\partial T_{\text{atm}}(p)}{\partial t} \Big|_{\text{rad}} + \frac{\partial T_{\text{atm}}(p)}{\partial t} \Big|_{\text{conv}} + \frac{\partial T_{\text{atm}}(p)}{\partial t} \Big|_{\text{adv}} \quad (1)$$

$$+ \frac{\partial T_{\text{atm}}(p)}{\partial t} \Big|_{\text{cond}} + \frac{\partial T_{\text{atm}}(p)}{\partial t} \Big|_{\text{diff}},$$

$$\frac{\partial T_s}{\partial t} = \frac{\partial T_s}{\partial t} \Big|_{\text{rad}} + \frac{\partial T_s}{\partial t} \Big|_{\text{conv}} + \frac{Q_s}{C_o} + \frac{Q_{\text{bias}}}{C_o}, \quad (2)$$

where t is time and p is pressure (with 30 pressure levels), and C_o is the heat capacity of a unit area of water with a depth of

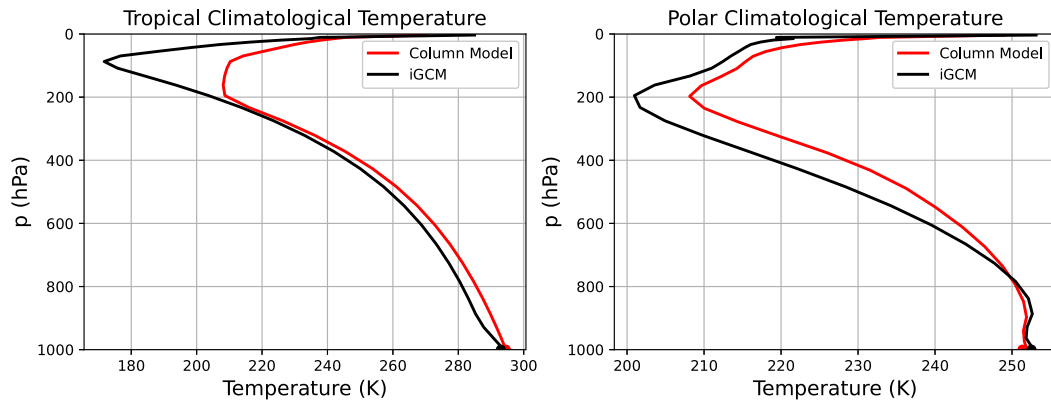


FIG. 2. Comparison between the single-column model (red) and idealized GCM (black) for the (a) tropical ($|\text{lat}| < 10^\circ$) climatological temperature and (b) polar ($\text{lat} > 80^\circ\text{N}$) climatological temperature.

1 m. The subscripts rad, conv, adv, cond, and diff refer to radiative, convective, advective, condensation, and diffusive temperature tendencies, respectively; Q_S is the imposed surface heat source term ($0, 12, 24 \text{ W m}^{-2}$) and Q_{bias} is a bias term described below. The radiative and convective sensible heat flux and latent heat flux temperature tendencies are computed interactively. The Rapid Radiative Transfer Model for GCMs (RRTMG) (Mlawer et al. 1997) radiation scheme is used for the computation of shortwave and longwave radiative temperature tendencies. The surface albedo and control insolation are set to idealized GCM values in the tropics (10°S – 10°N) and poleward of 80° . Convection is implemented as an adjustment of the temperature profile to the moist adiabat, whereas the idealized GCM uses a simplified Betts–Miller convection scheme (Frierson 2007). Note that at high latitudes, horizontal atmospheric energy transport induces a temperature structure stable to convection, and hence convection has no effect.

Values from the idealized GCM experiments averaged in the tropics (10°S – 10°N) and poleward of 80°N are used to prescribe the specific humidity profile, which affects the radiation. In addition, the time-mean advection and condensation temperature tendency profiles from the idealized GCM simulations are added as external temperature tendency terms to simulate the dry and moist components of atmospheric energy transport convergence respectively, and the diffusive temperature tendency term is prescribed from the idealized GCM boundary layer scheme (see Fig. S2 for the temperature tendency profiles). The advective temperature tendency term is calculated in the GCM as the difference in temperature tendency before and after running the dynamics module; hence, it contains the horizontal and vertical advection temperature tendencies and includes the effect of transient eddies. The SCM has no surface sensible and latent heat fluxes, but, unlike the GCM, the surface energy budget has a convection term [Eq. (2)], as the SCM convection scheme applies the same critical lapse rate between the ground and the first model level as it does between model levels (Manabe and Strickler 1964). Moreover, despite having the same TOA insolation and surface albedo as the GCM, there is a difference in absorbed shortwave radiation at the surface, which may be due to the

difference in the amount of absorbed shortwave radiation in the atmosphere by the two different radiation schemes. Hence, a bias term (Q_{bias}) is added to account for the difference between the GCM's surface turbulent (sensible and latent) heat fluxes and the SCM's surface convection term, and the bias in net surface shortwave radiation: $Q_{\text{bias}} = (\text{GCM surface turbulent heat flux} - \text{SCM surface convective heat flux}) + (\text{GCM absorbed shortwave at the surface} - \text{SCM absorbed shortwave at the surface})$. When we add a surface heat source (Q_S) at high latitudes in the idealized GCM, the surface turbulent heat fluxes are smaller, hence Q_{bias} is smaller. The values of Q_{bias} are tabulated in Table S1 in the online supplemental material.

The climatological temperature profiles of the idealized GCM and SCM are similar (Fig. 2). Similarities between the temperature profiles simulated by the idealized GCM and by the SCM still hold when the latitudinal bounds of the tropics are set to 20°S – 20°N and the high latitudes to 60° (see Fig. S3).

4. Attribution of idealized GCM tropical and polar lapse-rate changes to forcings and feedbacks

As discussed in the introduction, the forcing dependence of the high-latitude lapse-rate feedback makes a TOA budget approach to attributing the polar surface warming to different forcings and feedbacks ambiguous (see next section). The SCM allows us to attribute the idealized GCM's tropical and polar lapse-rate changes to the different forcings and feedbacks. The CO_2 concentration is a single value in the SCM, whereas the water vapor and atmospheric energy transport profiles (advection and condensation temperature tendencies in Fig. S2) are derived from the idealized GCM experiments. We individually perturb CO_2 , water vapor (in the radiative transfer scheme), atmospheric energy transport (moist and dry components), and vertical diffusion in the tropics and high latitudes to attribute the total warming to each of these individual components.

Figure 3 shows the decomposition of tropical and polar lapse-rate changes of the three idealized GCM perturbation

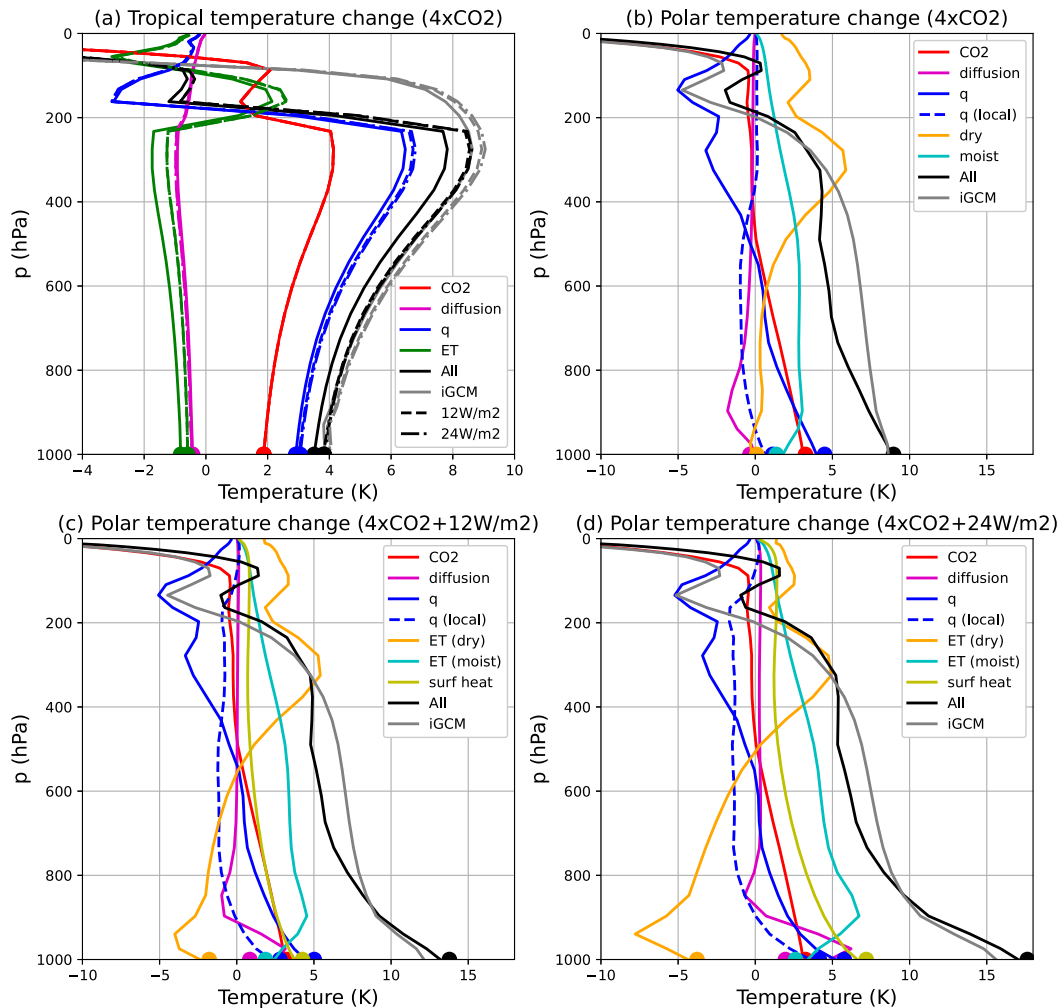


FIG. 3. (a) Tropical and (b)–(d) polar temperature change for the idealized GCM (gray) and three perturbation experiments using the single-column model: $4 \times \text{CO}_2$ in (a) and (b), $4 \times \text{CO}_2$ with 12 W m^{-2} surface heat source poleward of 80° in (a) and (c), and $4 \times \text{CO}_2$ with 24 W m^{-2} surface heat source poleward of 80° in (a) and (d). The SCM experiments with all changes (black) are exactly the same as the sum of individual changes and fit the idealized GCM (gray) well. The individual forcing and feedback contributions are calculated by individually perturbing them in the single-column model (colors). They include the CO_2 increase (red), the change in vertical diffusion (magenta), the water vapor feedback (blue), the “local” water vapor feedback (blue dashed; see section 6), the energy transport [green in tropics, separated into dry (orange) and moist (cyan) in high latitudes], and the surface heat source (yellow). The tropical temperature changes of the three experiments in (a) are similar enough to be plotted together (12 W m^{-2} using dashed lines and 24 W m^{-2} using dash-dotted lines). Surface temperature change attributions are summarized in Table 1.

experiments: $4 \times \text{CO}_2$, $4 \times \text{CO}_2$ with $Q_s = 12 \text{ W m}^{-2}$, and $Q_s = 24 \text{ W m}^{-2}$; Table 1 summarizes the surface temperature change attributions.

The tropical lapse-rate changes for the three experiments are similar enough to be plotted in the same figure (Fig. 3a): the $Q_s = 12 \text{ W m}^{-2}$ and $Q_s = 24 \text{ W m}^{-2}$ experiment changes are shown by dashed and dash-dotted lines respectively, and fall close to each other. The tropical lapse-rate changes are decomposed into the temperature change from the CO_2 forcing (red), changes due to vertical diffusion (magenta), the water vapor feedback (blue), and energy transport (green). For each

GCM experiment, the SCM’s response to applying all of the perturbations simultaneously (black) is exactly the same as the sum of the responses to the individual perturbations and fits the idealized GCM’s response well throughout the troposphere (gray), demonstrating the accuracy of the attribution method. Differences in the stratosphere between the SCM and idealized GCM may be due to the different radiation schemes or ozone distributions. Since convection is triggered in the tropics, the temperature profiles are moist adiabatic and the vertical structure of tropospheric temperature change ($\Delta T/\Delta T_s$) is approximately the same for all SCM experiments. The energy

TABLE 1. Surface temperature change attribution based on the single-column model decomposition for the three perturbation experiments. CO₂ and water vapor denote the radiative effect of their increase on surface temperature, whereas ET denotes the effect of the change in energy transport on surface temperature and is decomposed into its dry and moist components in the pole. Q_s denotes the effect of the surface heat source on the surface temperature change. Diffusion denotes the effect of the change in diffusive temperature tendency on surface temperature change. Units are K.

Forcing/feedback	$4 \times \text{CO}_2$	$4 \times \text{CO}_2 + 12 \text{ W m}^{-2}$	$4 \times \text{CO}_2 + 24 \text{ W m}^{-2}$
Tropics			
CO ₂	1.9	1.9	1.9
Water vapor	2.9	3.0	3.1
ET	-0.8	-0.6	-0.6
Diffusion	-0.43	-0.5	-0.5
Tropics total	3.5	3.8	3.8
Pole			
CO ₂	3.3	3.3	3.3
Water vapor	4.5	5.0	5.8
ET (dry)	0.1	-1.8	-3.8
ET (moist)	1.4	1.9	2.6
Diffusion	-0.3	0.9	2.0
Q_s	0	4.3	7.2
Pole total	9.0	13.8	17.6

transport is slightly reduced in the experiments with surface heat sources.

The polar lapse-rate changes (Figs. 3b–d) are decomposed into the temperature changes from the CO₂ forcing (red), the change in vertical diffusion (magenta), the water vapor feedback (blue), the “local” water vapor feedback (blue dashed; see section 6), the energy transport (dry component in orange and moist component in cyan), and the surface heat source (yellow). Again, for each GCM experiment, the SCM’s response to applying all of the perturbations simultaneously (black) is exactly the same as the sum of the responses to the individual perturbations, and fits the idealized GCM’s response well throughout the troposphere (gray), although not as well as in the tropics. Discrepancies between SCM (all) and the idealized GCM may be due to the lack of time fluctuations in the SCM. The increase in longwave absorbers (CO₂ and water vapor) leads to bottom-heavy warming, the dry component of energy transport leads to top-heavy warming, the moist component of energy transport leads to midtroposphere enhanced warming, and the surface heat source leads to very bottom-heavy warming.

The polar surface temperature change is 4.8 and 8.6 K higher in the $Q_s = 12 \text{ W m}^{-2}$ and $Q_s = 24 \text{ W m}^{-2}$ cases, respectively, compared to the $Q_s = 0 \text{ W m}^{-2}$ case, which is caused mainly by 4.3 and 7.2 K warming, respectively, due to the surface heat source. Reductions in the dry component of energy transport cause cooling of 1.8 and 3.8 K, respectively, versus a 0.1 K warming in the simulation with $Q_s = 0 \text{ W m}^{-2}$. There are also slight increases in warming due to the water vapor feedback (discussed in section 6), the moist component of the energy transport, and the diffusion term compared to the $4 \times \text{CO}_2$ experiment (Table 1). These results are consistent with Hwang et al. (2011), who found that enhanced Arctic warming due to local feedbacks weakens the equator-to-pole temperature gradient and reduces the dry component of the atmospheric energy transport, which outweighs the increase in the moist component of

atmospheric energy transport that arises from the enhanced warming. Alexeev and Jackson (2013) also found that a strong surface albedo feedback reduces the polar atmospheric heat transport convergence. The lapse-rate changes caused by changes in CO₂, water vapor, energy transport, and Q_s do not depend strongly on the inclusion of the vertical diffusion term in the SCM.

5. Surface temperature change attribution method comparison

The conventional surface temperature change attribution method (Pithan and Mauritsen 2014; Stuecker et al. 2018) computes the vertically uniform temperature change required to balance the top-of-atmosphere energy imbalance caused by each forcing and feedback, with any departures from vertically uniform warming collected into the lapse-rate feedback. The deviation from vertically uniform temperature change is then accounted for in the lapse-rate feedback. One can decompose the surface temperature changes in the idealized GCM experiments as follows [similar to Eq. (3) in the methods section of Stuecker et al. (2018)]:

$$\Delta T_S(\phi) = \left(-\frac{1}{\lambda_p} \right) \{ \Delta T_S(\phi) [\lambda'_p(\phi) + \lambda_{\text{LR}}(\phi) + \lambda_{\text{WV}}(\phi)] + Q_s(\phi) + \mathcal{F}(\phi) + \Delta[\nabla \cdot \mathbf{F}(\phi)] \} \quad (3)$$

where ϕ is the latitude. The surface temperature change attributions are then given by the average of $\Delta T_S(\phi)$ over the tropics and Arctic. The Planck feedback is decomposed into its global-mean $\overline{\lambda_p}$ and its deviation λ'_p , λ_{LR} is the lapse-rate feedback, λ_{WV} is the water vapor feedback, Q_s is the surface forcing, and there would be an additional cloud feedback term if analyzing a comprehensive GCM.

To apply the conventional attribution method to the GCM simulations, we use aquaplanet kernels derived from Isca

(Vallis et al. 2018; Liu 2020) to calculate the feedbacks.¹ The CO₂ forcing \mathcal{F} is computed as the change in TOA net radiation between the control simulation and an idealized GCM simulation where sea surface temperatures (SSTs) are fixed to the control SST and CO₂ concentrations are quadrupled (Hansen et al. 2005). The change in atmospheric energy transport convergence $\Delta(\nabla \cdot \mathbf{F})$ is computed as the change in net TOA radiation (minus the surface forcing) between the control and perturbed simulations. This method of attributing surface temperature changes to forcings and feedbacks then tells us how much surface temperature change is required to balance the TOA energy imbalance caused by each forcing or feedback, assuming the atmospheric temperature change is vertically uniform (except for the lapse-rate feedback). There is no explicit vertical diffusion in this TOA energy budget approach, in contrast to the vertically resolved CFRAM, so we do not include it in our comparison between SCM and TOA budget approach.

Figure 4 compares this TOA energy budget surface temperature change attribution method (crosses) with the single-column model based attribution method (filled circles) for $4 \times \text{CO}_2$ (Fig. 4a) and for $4 \times \text{CO}_2$ with $Q_s = 12 \text{ W m}^{-2}$ (Fig. 4b) and with $Q_s = 12 \text{ W m}^{-2}$ (Fig. 4c). The tropical (x axis; 10°S to 10°N) and polar (y axis; 80° to 90°N) attributions are plotted against each other. If a point falls above (below) the one-to-one line, the forcing or feedback contributes to polar (tropical) amplification. As in Pithan and Mauritsen (2014), the TOA attribution method suggests that the Planck feedback, the lapse-rate feedback, and increased horizontal energy transport are the primary drivers of polar amplification. The lapse-rate feedback contributes to more polar amplification in the surface heat source experiments. The single-column model attribution method, in contrast, has no temperature feedback in its decomposition. Since the TOA energy budget method assumes that the temperature response to a TOA energy imbalance is vertically uniform, it will attribute a larger (smaller) amplitude change in surface temperature than the single-column model if the response to the forcing or feedback is top-heavy (bottom-heavy). In the tropics, all temperature changes are top-heavy as they follow the moist adiabat, and hence the SCM attributions are all closer to the y axis than the corresponding TOA method attributions. In the high latitudes, the SCM temperature changes from increases in CO₂, water vapor, and surface heat source are bottom-heavy, so they all contribute a larger surface temperature change than is diagnosed from the TOA method. The energy transport convergence change leads to top-heavy warming; therefore, the warming attributed to it by the SCM method is smaller than the warming attributed by the TOA method, and even negative in the surface heat source cases. The residual term (black), calculated as the difference between the sum of each term and the actual surface temperature change, is small for all the simulations.

¹ Using aquaplanet kernels derived from the GFDL Atmospheric Model 2 leads to strong biases in the tropics due to its different mean state.

In summary, we underline two main points from this comparison of the single-column model and TOA-based surface temperature change attribution methods:

- The increase in longwave absorbers (CO₂ and water vapor) goes from contributing to tropical amplification in the TOA attribution method to contributing to polar amplification in the SCM attribution method. The forcing from CO₂ and the water vapor feedback are stronger in the tropics than the high latitudes, but since the tropical SCM attribution includes the effect of convection, the warming maximum shifts into the upper troposphere and there is less surface warming. In the high latitudes, however, an increase in longwave absorbers leads to bottom-heavy warming (Taylor et al. 2013; Cronin and Jansen 2016; Henry and Merlis 2020). Russotto and Biasutti (2020) analyze the response of atmospheric GCMs using a moist energy balance model, and similarly find that a tropically amplified CO₂ forcing and water vapor feedback lead to a polar-amplified temperature response.
- Since the increase in atmospheric energy transport convergence preferentially affects the midtroposphere, it leads to less surface warming at high latitudes, and even to surface cooling in the surface heat source experiments. In contrast, the effect of the vertically integrated increase in atmospheric energy transport convergence would always be a surface warming in the TOA-budget based approach.

6. Local and remote drivers of temperature change

The SCM attribution method can also be used to decompose polar amplification into its local and remote drivers. The CO₂ and surface heat source perturbations are local drivers, while the energy transport can be considered as a remote driver. The water vapor feedback includes both local and remote contributions. First, the change in specific humidity can be decomposed into a temperature-dependent change and a change due to relative humidity: $\Delta q = \Delta q|_{\text{fixedRH}} + \Delta \text{RH} \times q^*|_{\text{clim}}$, where $q^*|_{\text{clim}}$ is the climatological saturation specific humidity. Since the relative humidity in the idealized GCM stays relatively constant (Fig. S4), we ignore the second term of this equation. Using fixed relative humidity (RH) SCM experiments, we can decompose the temperature-dependent changes in specific humidity into the “local” changes in response to the temperature changes forced by increased CO₂ and the surface heat source, and the “remote” changes in response to the temperature change forced by altered energy transports: $\Delta q \approx \Delta q|_{\text{fixedRH}} = \Delta q|_{\text{fixedRH}, \Delta \text{CO}_2, \Delta Q_s} + \Delta q|_{\text{fixedRH}, \Delta \text{ET}}$.

This local versus remote decomposition of the water vapor concentration increase is not perfect, as it assumes the energy transport simply affects the humidity of the high latitudes by changing its temperature and activating the local water vapor feedback, whereas the general circulation can directly advect water vapor. The energy transport term also contains vertical advection, which can change as a result of local diabatic forcings (shown in magenta in Fig. S2). Moreover, GCM experiments where the forcing from a CO₂ increase is constrained to the high latitudes show changes in energy transport, which

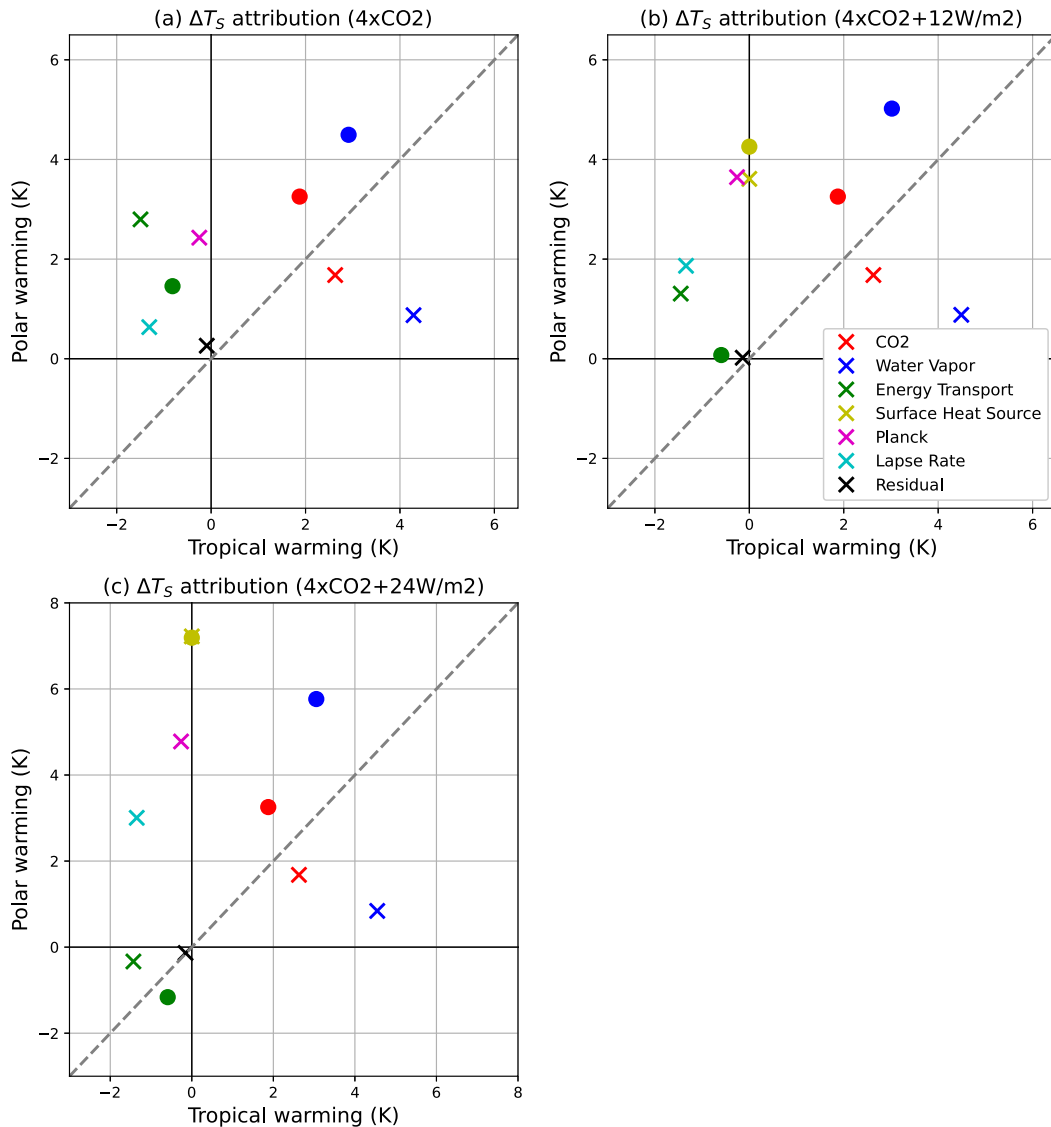


FIG. 4. Surface temperature change attributions for (a) $4 \times \text{CO}_2$ and for $4 \times \text{CO}_2$ with (b) $Q_s = 12 \text{ W m}^{-2}$ and (c) $Q_s = 24 \text{ W m}^{-2}$ using the TOA energy budget method (crosses) and the SCM method presented in this paper (dots). Presented are the surface temperature change attributions to the increase in CO_2 (red), water vapor (blue), energy transport (green), and surface heat source (yellow) for both methods. The Planck (magenta) and lapse-rate (cyan) feedback contributions are also shown for the TOA energy budget method. The residual term (black) is calculated as the difference between the sum of each term of the TOA energy budget method and the actual surface temperature change. When the point is above (below) the one-to-one line, the forcing or feedback contributes to polar (tropical) amplification.

would also affect the water vapor feedback (Stuecker et al. 2018). Since energy transport is affected by both temperature and humidity gradients, it is not clear that any perfect local/remote decomposition exists. Nevertheless, our definition of “local” recovers traditional SCM treatments of fixed relative humidity water vapor feedback (Manabe and Wetherald 1967) in the limit of no changes in energy transport.

The fixed-RH SCM simulations have the same modules and parameters as the standard SCM simulations, but instead of prescribing the idealized GCM’s specific humidity, they have

fixed relative humidity and the specific humidity is free to evolve with temperature. The climatological temperature of the fixed RH SCMs have a warm bias (Fig. S5) and the climatological specific humidity is biased high (Fig. S6). We do two sets of fixed-RH SCM experiments: the first (local) experiment is forced with the increase in CO_2 concentration (and surface heat source), and the second is forced with increased CO_2 concentration (and surface heat source) and perturbed energy transport. The latter has less tropical warming and similar polar warming compared to the idealized GCM (red

TABLE 2. Surface temperature change attribution based on the single-column model decomposition for the three perturbation experiments. The tropical surface temperature change attributions are sufficiently similar to be in a single column. The three successive values separated by a comma refer to the $4 \times \text{CO}_2$, $Q_s = 12 \text{ W m}^{-2}$, and $Q_s = 24 \text{ W m}^{-2}$ experiments, respectively. Discrepancies between the total and the sum of local and remote totals occur as the total is the surface temperature change from the experiment with all perturbations. Units are K.

Forcing/feedback	Tropics	Pole ($4 \times \text{CO}_2$)	Pole ($4 \times \text{CO}_2 + 12 \text{ W m}^{-2}$)	Pole ($4 \times \text{CO}_2 + 24 \text{ W m}^{-2}$)
CO_2	1.9	3.3	3.3	3.3
q (local)	10.3	1.1	2.8	4.2
Q_s	0	0	4.3	7.2
Diffusion	-0.4	-0.3	0.9	2.0
Local total	11.8	4.0	11.2	16.6
q (remote)	-7.4, -7.3, -7.3	3.4	2.2	1.6
ET	-0.8, -0.6, -0.6	1.5	0.1	-1.2
Remote total	-8.2, -7.9, -7.9	4.8	2.3	0.5
Total	3.5, 3.8, 3.8	9.0	13.8	17.6

lines in Fig. S7 for the $4 \times \text{CO}_2$ experiment), and similar changes in specific humidity in the tropics and a higher increase in high latitudes compared to the idealized GCM (red lines in Fig. S8 for the $4 \times \text{CO}_2$ experiment). The local (as defined above) increase in water vapor, $\Delta q|_{\text{fixedRH}, \Delta \text{CO}_2, \Delta Q_s}$, is taken to be the change in water vapor from the first set of fixed-RH SCM experiments (blue lines in Fig. S8 for the $4 \times \text{CO}_2$ experiment), and the remote (as defined above) increase in water vapor, $\Delta q|_{\text{fixedRH}, \Delta \text{ET}}$, is taken to be the residual between the total change in water vapor and the local change in water vapor. We then force the original SCM with the local and remote specific humidity changes to deduce the q (local) and q (remote) temperature changes (shown in Table 2). The q (local) experiments are comparable to the fixed RH experiments in Payne et al. (2015). The temperature changes from the high-latitude q (local) experiments are shown in Fig. 3 (blue dashed).

Table 2 summarizes the result of this local and remote decomposition of surface temperature change. In the three perturbation experiments, the warming from CO_2 alone is 1.9 K in the tropics and 3.3 K at high latitudes, and hence increasing CO_2 leads to polar amplification in the absence of any feedbacks. The addition of the local water vapor feedback increases the tropical surface warming to 12.2 K and the polar surface warming to 4.4 K in the $4 \times \text{CO}_2$ experiment, and thus cancels the polar amplification from CO_2 alone. Payne et al. (2015) also found a tropical amplification of surface temperature change in their fixed-RH SCM simulations, although with somewhat different magnitude. Finally, adding the atmospheric energy transport and its implied water vapor change decreases the tropical surface warming to 3.5 K, and increases the polar surface warming to 9.0 K in the $4 \times \text{CO}_2$ experiment, thus leading to polar amplification. The polar surface heat source generally increases the amount of polar amplification despite the partial compensation by a reduction in dry energy transport. For the $4 \times \text{CO}_2$ experiment, approximately half of the polar warming is due to local sources (4.0 K out of 9 K of total warming), but the polar-amplified pattern of warming is primarily caused by the increase in atmospheric energy transport which cools the tropics and warms the high latitudes. The high-latitude warming is then strongly enhanced by the increased water vapor from remote

sources. When a polar surface heat source is added, almost all of the polar surface warming is due to local sources because of the surface heat source and the compensating reduction in the dry component of energy transport: 11.2 and 16.6 K from local sources for a total warming of 13.8 and 17.6 K for the $Q_s = 12 \text{ W m}^{-2}$ and $Q_s = 24 \text{ W m}^{-2}$ experiments, respectively.

7. Summary and discussion

Unlike the tropics, which are close to radiative–convective equilibrium, the high latitudes are in radiative–advective equilibrium: different forcings and feedbacks induce different lapse-rate responses. Previous surface temperature change attribution methods compute the vertically uniform temperature change required to balance the top-of-atmosphere energy imbalance caused by each forcing and feedback, with any departures from vertically uniform warming collected into the lapse-rate feedback. In these attributions, the lapse-rate feedback functions as a residual that cannot be clearly ascribed to any particular physical process.

We introduce a surface temperature change attribution method based on a single-column model, which accounts for the vertically inhomogeneous temperature change contributions of each forcing and feedback. We find that the warming from increased longwave absorbers (CO_2 and water vapor) is bottom-heavy and accounts for most of the surface warming at high latitudes in the absence of a surface heat source. By contrast, the warming from atmospheric heat transport preferentially warms the middle and upper troposphere. The CFRAM method (Taylor et al. 2013) previously found that the warming from increased CO_2 and water vapor leads to bottom-heavy warming at high latitudes, and that convection leads to top-heavy warming at low latitudes. The single-column model has the additional feature of enabling an analysis of how different processes interact with one another. Convection responds to radiative destabilization, which is particularly relevant in low latitudes (Wang and Huang 2020). When a polar surface heat source is added, there is a reduction in the dry component of atmospheric energy transport that partially compensates for the extra surface warming from the polar surface heat source.

Compared to the conventional surface temperature change attribution method, the increase in longwave absorbers (CO₂ and water vapor) goes from contributing to tropical amplification to polar amplification. In addition, the polar warming contribution from the increase in atmospheric energy transport convergence is reduced as it preferentially warms the middle and upper troposphere. Moreover, when a polar surface heat source is added, the contributions of the surface heat source and the concomitant reduction in atmospheric energy transport are properly separated instead of producing a larger lapse-rate feedback contribution to polar amplification.

Finally, we separated the drivers of atmospheric temperature change into local and remote contributors and found that, in the absence of a polar surface heat source, the change in energy transport and the “remote” water vapor changes were primarily responsible for the polar-amplified pattern of warming. The addition of a polar surface heat source increases the contribution of local drivers to polar warming at the expense of remote drivers, as the dry energy transport is reduced.

It is important to note that clouds and sea ice were ignored in this analysis (aside from the surface heat source that mimics the effects of shortwave cloud feedbacks and sea ice), although they may play an important role in explaining the pattern of surface temperature change in comprehensive climate model simulations. Arctic amplification also has seasonality—it is strong in winter and suppressed in summer—which has been suggested to result from the increased polar ocean heat uptake in summer and ocean heat release in winter from the melting sea ice (Manabe and Stouffer 1980; Bintanja and van der Linden 2013; Dai et al. 2019). Nevertheless, we believe that the single-column model can be a stepping stone for connecting simple physical models with comprehensive climate models: clouds and seasonality can be prescribed in the SCM, which would be a valuable extension of the present work. This would allow us to understand the basic mechanisms driving Arctic amplification.

Acknowledgments. The code and data needed to reproduce all figures, tables, and supplemental figures are available at https://github.com/matthewjhenry/HMLR19_SCM. Documentation for the Python ClimLab package can be found at <https://climlab.readthedocs.io/>. The top-of-atmosphere albedo data from the Cloud and the Earth’s Radiant Energy System (CERES) can be found at <https://ceres.larc.nasa.gov/>. The CMIP6 data are available on the Earth System Grid Federation database. This work was supported by a Natural Sciences and Research Council (NSERC) Discovery grant and Canada Research Chair, as well as a Compute Canada allocation. B.E.J.R. was supported by NSF Grant AGS-1455071.

REFERENCES

- Abbot, D. S., and E. Tziperman, 2008: Sea ice, high-latitude convection, and equable climates. *Geophys. Res. Lett.*, **35**, L03702, <https://doi.org/10.1029/2007GL032286>.
- Alexeev, V. A., and C. H. Jackson, 2013: Polar amplification: Is atmospheric heat transport important? *Climate Dyn.*, **41**, 533–547, <https://doi.org/10.1007/s00382-012-1601-z>.
- Anderson, J. L., and Coauthors, 2004: The new GFDL global atmosphere and land model AM2–LM2: Evaluation with prescribed SST simulations. *J. Climate*, **17**, 4641–4673, <https://doi.org/10.1175/JCLI-3223.1>.
- Bintanja, R., and E. van der Linden, 2013: The changing seasonal climate in the Arctic. *Sci. Rep.*, **3**, 1556, <https://doi.org/10.1038/srep01556>.
- Cronin, T. W., and M. F. Jansen, 2016: Analytic radiative-advective equilibrium as a model for high-latitude climate. *Geophys. Res. Lett.*, **43**, 449–457, <https://doi.org/10.1002/2015GL067172>.
- Dai, A., D. Luo, M. Song, and J. Liu, 2019: Arctic amplification is caused by sea-ice loss under increasing CO₂. *Nat. Commun.*, **10**, 121, <https://doi.org/10.1038/s41467-018-07954-9>.
- Eyring, V., S. Bony, G. A. Meehl, C. A. Senior, B. Stevens, R. J. Stouffer, and K. E. Taylor, 2016: Overview of the Coupled Model Intercomparison Project Phase 6 (CMIP6) experimental design and organization. *Geosci. Model Dev.*, **9**, 1937–1958, <https://doi.org/10.5194/GMD-9-1937-2016>.
- Feldl, N., and S. Bordoni, 2016: Characterizing the Hadley circulation response through regional climate feedbacks. *J. Climate*, **29**, 613–622, <https://doi.org/10.1175/JCLI-D-15-0424.1>.
- , B. T. Anderson, and S. Bordoni, 2017: Atmospheric eddies mediate lapse rate feedback and Arctic amplification. *J. Climate*, **30**, 9213–9224, <https://doi.org/10.1175/JCLI-D-16-0706.1>.
- , S. Po-Chedley, H. K. Singh, S. Hay, and P. J. Kushner, 2020: Sea ice and atmospheric circulation shape the high-latitude lapse rate feedback. *npj Climate Atmos. Sci.*, **3**, 41, <https://doi.org/10.1038/S41612-020-00146-7>.
- Frierson, D. M., 2007: The dynamics of idealized convection schemes and their effect on the zonally averaged tropical circulation. *J. Atmos. Sci.*, **64**, 1959–1976, <https://doi.org/10.1175/JAS3935.1>.
- , I. M. Held, and P. Zurita-Gotor, 2006: A gray-radiation aquaplanet moist GCM. Part I: Static stability and eddy scale. *J. Atmos. Sci.*, **63**, 2548–2566, <https://doi.org/10.1175/JAS3753.1>.
- Hansen, J., and Coauthors, 2005: Efficacy of climate forcings. *J. Geophys. Res.*, **110**, D18104, <https://doi.org/10.1029/2005JD005776>.
- Henry, M., and T. M. Merlis, 2020: Forcing dependence of atmospheric lapse rate changes dominates residual polar warming in solar radiation management climate scenarios. *Geophys. Res. Lett.*, **47**, e2020GL087929, <https://doi.org/10.1029/2020GL087929>.
- Hwang, Y.-T., and D. M. Frierson, 2010: Increasing atmospheric poleward energy transport with global warming. *Geophys. Res. Lett.*, **37**, L24807, <https://doi.org/10.1029/2010GL045440>.
- , —, and J. E. Kay, 2011: Coupling between Arctic feedbacks and changes in poleward energy transport. *Geophys. Res. Lett.*, **38**, L17704, <https://doi.org/10.1029/2011GL048546>.
- Jucker, M., and E. Gerber, 2017: Untangling the annual cycle of the tropical tropopause layer with an idealized moist model. *J. Climate*, **30**, 7339–7358, <https://doi.org/10.1175/JCLI-D-17-0127.1>.
- Laliberté, F., and P. Kushner, 2013: Isentropic constraints by midlatitude surface warming on the Arctic midtroposphere. *Geophys. Res. Lett.*, **40**, 606–611, <https://doi.org/10.1029/2012GL054306>.
- Liu, Q., 2020: Radiative kernels for Isca v1.0. Zenodo, <https://doi.org/10.5281/zenodo.4282681>.
- Loeb, N. G., and Coauthors, 2018: Clouds and the Earth’s Radiant Energy System (CERES) Energy Balanced and Filled (EBAF) top-of-atmosphere (TOA) edition-4.0 data product. *J. Climate*, **31**, 895–918, <https://doi.org/10.1175/JCLI-D-17-0208.1>.
- Lu, J., and M. Cai, 2009: A new framework for isolating individual feedback processes in coupled general circulation climate models. Part I: Formulation. *Climate Dyn.*, **32**, 873–885, <https://doi.org/10.1007/s00382-008-0425-3>.

- Manabe, S., and R. F. Strickler, 1964: Thermal equilibrium of the atmosphere with a convective adjustment. *J. Atmos. Sci.*, **21**, 361–385, [https://doi.org/10.1175/1520-0469\(1964\)021<0361:TEOTAW>2.0.CO;2](https://doi.org/10.1175/1520-0469(1964)021<0361:TEOTAW>2.0.CO;2).
- , and R. T. Wetherald, 1967: Thermal equilibrium of the atmosphere with a given distribution of relative humidity. *J. Atmos. Sci.*, **24**, 241–259, [https://doi.org/10.1175/1520-0469\(1967\)024<0241:TEOTAW>2.0.CO;2](https://doi.org/10.1175/1520-0469(1967)024<0241:TEOTAW>2.0.CO;2).
- , and R. J. Stouffer, 1980: Sensitivity of a global climate model to an increase of CO₂ concentration in the atmosphere. *J. Geophys. Res.*, **85**, 5529–5554, <https://doi.org/10.1029/JC085iC10p05529>.
- , —, M. Spelman, and K. Bryan, 1991: Transient responses of a coupled ocean–atmosphere model to gradual changes of atmospheric CO₂. Part I: Annual mean response. *J. Climate*, **4**, 785–818, [https://doi.org/10.1175/1520-0442\(1991\)004<0785:TROACO>2.0.CO;2](https://doi.org/10.1175/1520-0442(1991)004<0785:TROACO>2.0.CO;2).
- Merlis, T. M., T. Schneider, S. Bordoni, and I. Eisenman, 2013: Hadley circulation response to orbital precession. Part I: Aquaplanets. *J. Climate*, **26**, 740–753, <https://doi.org/10.1175/JCLI-D-11-00716.1>.
- Mlawer, E. J., S. J. Taubman, P. D. Brown, M. J. Iacono, and S. A. Clough, 1997: Radiative transfer for inhomogeneous atmospheres: RRTM, a validated correlated-*k* model for the longwave. *J. Geophys. Res.*, **102**, 16 663–16 682, <https://doi.org/10.1029/97JD00237>.
- Payne, A. E., M. F. Jansen, and T. W. Cronin, 2015: Conceptual model analysis of the influence of temperature feedbacks on polar amplification. *Geophys. Res. Lett.*, **42**, 9561–9570, <https://doi.org/10.1002/2015GL065889>.
- Pithan, F., and T. Mauritsen, 2014: Arctic amplification dominated by temperature feedbacks in contemporary climate models. *Nat. Geosci.*, **7**, 181–184, <https://doi.org/10.1038/ngeo2071>.
- Roe, G. H., N. Feldl, K. C. Armour, Y.-T. Hwang, and D. M. Frierson, 2015: The remote impacts of climate feedbacks on regional climate predictability. *Nat. Geosci.*, **8**, 135–139, <https://doi.org/10.1038/ngeo2346>.
- Rose, B. E., 2018: CLIMLAB: A Python toolkit for interactive, process oriented climate modeling. *J. Open Source Software*, **3**, 659, <https://doi.org/10.21105/joss.00659>.
- Rugenstein, M., and Coauthors, 2019: LongRunMIP: Motivation and design for a large collection of millennial-length AO-GCM simulations. *Bull. Amer. Meteor. Soc.*, **100**, 9861–9869, <https://doi.org/10.1175/BAMS-D-19-0068.1>.
- Russotto, R. D., and M. Biasutti, 2020: Polar amplification as an inherent response of a circulating atmosphere: Results from the TRACMIP aquaplanets. *Geophys. Res. Lett.*, **47**, e2019GL086771, <https://doi.org/10.1029/2019GL086771>.
- Screen, J. A., C. Deser, and I. Simmonds, 2012: Local and remote controls on observed Arctic warming. *Geophys. Res. Lett.*, **39**, L10709, <https://doi.org/10.1029/2012GL051598>.
- Shaw, T. A., and Z. Tan, 2018: Testing latitudinally dependent explanations of the circulation response to increased CO₂ using aquaplanet models. *Geophys. Res. Lett.*, **45**, 9861–9869, <https://doi.org/10.1029/2018GL078974>.
- Stocker, T. F., and Coauthors, 2013: Technical summary. *Climate Change 2013: The Physical Science Basis*, T. F. Stocker et al., Eds., Cambridge University Press, 33–115.
- Stuecker, M. F., and Coauthors, 2018: Polar amplification dominated by local forcing and feedbacks. *Nat. Climate Change*, **8**, 1076–1081, <https://doi.org/10.1038/s41558-018-0339-y>.
- Taylor, P. C., M. Cai, A. Hu, J. Meehl, W. Washington, and G. J. Zhang, 2013: A decomposition of feedback contributions to polar warming amplification. *J. Climate*, **26**, 7023–7043, <https://doi.org/10.1175/JCLI-D-12-00696.1>.
- Vallis, G. K., and Coauthors, 2018: Isca, v1.0: A framework for the global modelling of the atmospheres of Earth and other planets at varying levels of complexity. *Geosci. Model Dev.*, **11**, 843–859, <https://doi.org/10.5194/gmd-11-843-2018>.
- Wang, Y., and Y. Huang, 2020: Understanding the atmospheric temperature adjustment to CO₂ perturbation at the process level. *J. Climate*, **33**, 787–803, <https://doi.org/10.1175/JCLI-D-19-0032.1>.